# Carbon-in-$Al_4C_3$ Nanowire Superstructures for Field Emitters

**Yong Sun,[†] Hao Cui,[†,‡] Li Gong,[§] Jian Chen,[§] Juncong She,[†] Yanming Ma,[⊥] Peikang Shen,[†,‡] and Chengxin Wang[†,‡,*]**

[†]State Key Laboratory of Optoelectronic Materials and Technologies, School of Physics Science and Engineering, Sun Yat-sen (Zhongshan) University, Guangzhou 510275, People's Republic of China, [‡]The Key Laboratory of Low-Carbon Chemistry and Energy Conservation of Guangdong Province, Sun Yat-sen (Zhongshan) University, Guangzhou 510275, People's Republic of China, [§]Instrumental Analysis and Research Center, Sun Yat-sen (Zhongshan) University, Guangzhou 510275, People's Republic of China, and [⊥]State Key Laboratory of Superhard Materials, Jilin University, Changchun 130012, People's Republic of China

**ABSTRACT** As a kind of ionic (or salt-like) carbide, for $Al_4C_3$, hardly any active functions have been found except for structure material purposes. However, considering the unique characteristic features of its crystal structure, we think $Al_4C_3$ in fact might have huge potential for exhibiting active functionality on field-emission applications. Herein, we report the feasibility to approach such emitters by creating $Al_4C_3$-based nanowire superstructures. The conductive amorphous carbon (a-C) nanolayers are embedded quasi-periodically in $Al_4C_3$ nanowire and generate essential electrical contact to the insulating $Al_4C_3$. The superstructures acting as cold electron emitters display excellent field emission performance with the turn-on field as low as 0.65−1.3 V/$\mu$m and the threshold field down to 2.1−2.6 V/$\mu$m. We speculate that the emission characteristics, which are ever better than carbon nanotubes, are attributed to the unique crystal structure of $Al_4C_3$ and the enhanced electrons transport in the nanowires due to the existence of a-C nanolayers. Such emitters are technologically useful, because they can be easily fabricated on large substrates, and the synthesis process is simple and broadly applicable. The findings conceptually provide new opportunities for the application of $Al_4C_3$ ceramic material in vacuum microelectronic devices.

**KEYWORDS:** carbon-in-$Al_4C_3$ · nanowire superstructures · emitters · ceramic material · vacuum microelectronic devices

High-performance cold cathodes possessing a low turn-on field and a high emission current are strongly desired for the applications in field emission (FE) based devices such as field-emission displays and vacuum microelectronic devices.[1] With the advent of carbon nanotubes and various anisotropic nanostructured materials, there has been an upsurge in the interest in designing new FE based devices, because their tips with small curvature radius and large number of emitting centers per unit area could enhance the density of electron emission.[1] However, most of these researches were focused on carbon-based materials in simple substance or covalent-bond semiconductors materials, because they might possess a negative electron affinity (NEA) if the minimum energy of electrons in the conduction band is above the minimum energy of electrons in vacuum.[2] Investigations on the FE of other nanoscale materials are relatively lack. In particular, electron field emission from ionic carbides composed of highly electropositive elements (such as the alkali metals and aluminum) and carbon has not been reported before.

As an important ceramic material, $Al_4C_3$ (ionic carbide) is now known as the only intermediate compound in C−Al system, commonly applied as structure material such as reinforcement in aluminum−matrix composite materials, is mainly fabricated by mechanical alloying.[3−6] Usually, the $Al_4C_3$ phase is an undesired degradation product that is well-known to be not only brittle, but also highly sensitive to moisture contact and, thus, promote accelerated fatigue crack growth rates.[7] Although $Al_4C_3$ appears only to have passive functions only useful for structural material purposes, it in fact might have huge potential for exhibiting active functionality on FE devices if its unique crystal structure is fully utilized.

Now, let us consider what is unique about $Al_4C_3$. We think there are two characteristic features in $Al_4C_3$ structure: One is that the carbon atoms are present in the lattice as discrete carbon anions, $C^{4-}$, which is a very strong base and could hydrolyze to give methane gas.[8] This indicates that $C^{4-}$ easily gives up an electron, which exhibits behavior comparable to the alkali metals. Another characteristic feature is that $Al_4C_3$ has a rhombohedral structure (space group $R3m$), which can be described as a layered structure formed by alternated $Al_2C$ and $Al_2C_2$ layers or as the stacking of $Al_4C_3$ segments in the $c$-direction, which is shown in Figure 1a.[9] This determines that the aluminum atoms have the tetrahedral carbon coordination which is advantageous in reducing localization behavior of 3$p$ electrons on Al atoms, because there is no nonbonding level on an Al atom in the coordination structure.[10] Based on these characteristic features, we think that it is possible to extract

*Address correspondence to wchengx@mail.sysu.edu.cn.

Received for review August 26, 2010 and accepted January 5, 2011.

**Published online January 13, 2011**
**10.1021/nn102173b**

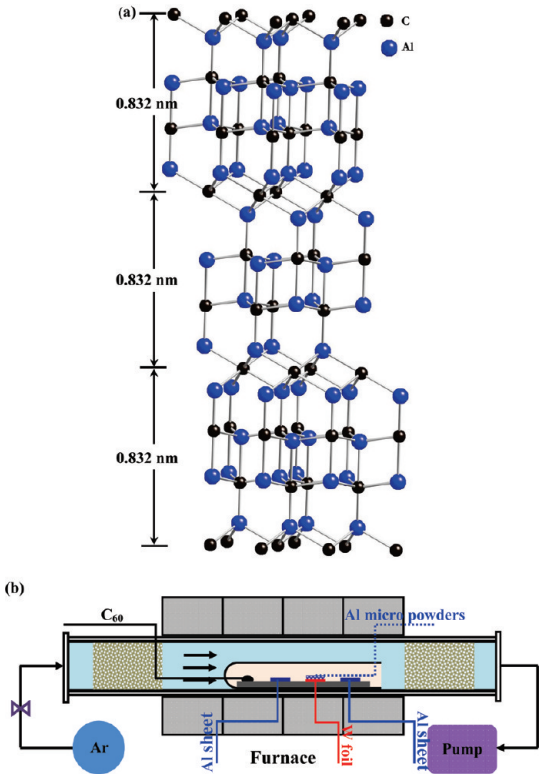


**Figure 1. (a) Structure of $Al_4C_3$; the structure is formed by alternating $Al_2C$ and $Al_2C_2$ layers, and the aluminum atoms have the tetrahedral carbon coordination. (b) The schematic diagram of the setup for the nanowire superstructures production.**

electrons from $Al_4C_3$ surface by applying a very low electric field and subsequently realize $Al_4C_3$ active functionality on FE devices. On the basis of this belief, the fabrication and FE applied research of $Al_4C_3$ nanostructures are exploring in our group.

However, to achieve the above goal, we have to solve two critical problems of practical application, namely, to enhance the electrons transport from bottom to top along the nanostructures ($Al_4C_3$ is an insulator at room temperature) and to prevent $Al_4C_3$ from hydrolyzing. Here we describe an efficient strategy for overcoming the bottlenecks mentioned above *via* the synthesis of amorphous carbon-in-$Al_4C_3$ nanowires sheathed with $Al_2O_3$ thin layers during vapor–solid (VS) growth. The finding in the excellent field-emission behavior, which is comparable to carbon nanotubes demonstrates that these promising nanowire superstructures can be used in a FE device. The present synthetic approach is direct and simple, provides a solution for the fabrication of functional 1-D hybrid nanowire FE devices, and opens new prospects in vacuum microelectronic devices application of $Al_4C_3$ ceramic material.

## RESULTS AND DISCUSSION

The morphologies of the as-prepared products are characterized by SEM, as shown in Figure 2a,b. Figure 2a shows the typical low-magnification SEM image of the large area nanowires grown on the stacked microballs, which do not cover the W substrate completely. The magnified images clearly reveal that the products grow radiately from the microballs and display uniform wire-shaped morphologies with a diameter of about 60 nm and a length of several micrometers, as shown in Figure 2b and the inset. Under the nanowires, microballs with diameter 1−2 $\mu$m always exist, as noted later, which indicates the microballs might have a critical induced effect on the nanowires growth. The structural analysis of as-grown product was further carried out using X-ray diffraction (XRD, Bruker D8 Advance) method. Figure 2c shows the diffraction peaks marked in red lines can be readily indexed to rhombohedral structure $Al_4C_3$ (JCPDS No. 35-0799) and other phases such as $W_2C$, W, and $Al_2O_3$ were also detected and designated out employing colored lines as shown. The W and $W_2C$ phase come from the substrate and compound formed by the reaction of W and C at high temperature, respectively. In addition, the typical broad band in low angle area up to 30 degrees is the characteristic of amorphous carbon.[11]

Besides, the sample was investigated employing the Raman method. The experimental measurement of Raman spectra was performed on Laser Raman Spectrometer (Renishaw inVia). Moreover, *ab initio* calculations were carried out using the plane-wave pseudopotential method within the linear response density functional theory through the Quantum-ESPRESSO package.[12] According to our calculations and analysis, six Raman-active modes ($3E_g + 3A1g$) were confirmed. Figure 3 exhibits our results of experimental measurement and *ab initio* calculation. A comparison of the two curves indicates that experiment spectra and theoretical results correspond very well. Shift of several $cm^{-1}$ between the two curves maybe origins from crystal defects and the optimizing process of $Al_4C_3$ lattice constant. Moreover, the inset in Figure 3 shows *D* and *E* peaks of carbon, which are located at 1352 and 1593 $cm^{-1}$.

The as-prepared products were sonicated and dispersed in ethanol solution for 20 min and then collected by copper mesh for STEM, TEM, and EDS line scan and mapping analysis. Figure 4a shows a *Z*-contrast STEM image of a single nanowire in the same sample of Figure 2a. One can see that the image displays a clear difference in the optical contrast. If there are no large changes in thickness at very short length scales, which is usually true for small areas in TEM samples, the intensity difference in an image such as Figure 4a comes from differences in chemical composition of local sample.[13] To clarify the composition of the nanowire, the line scan EDX analyses of the nanowire along the longitudinal and radial axis have been carried out (in parts b−d of Figure 3). Figure 3b shows a corresponding line scan spectrum of a nanowire along longitudinal axis and displays a periodic

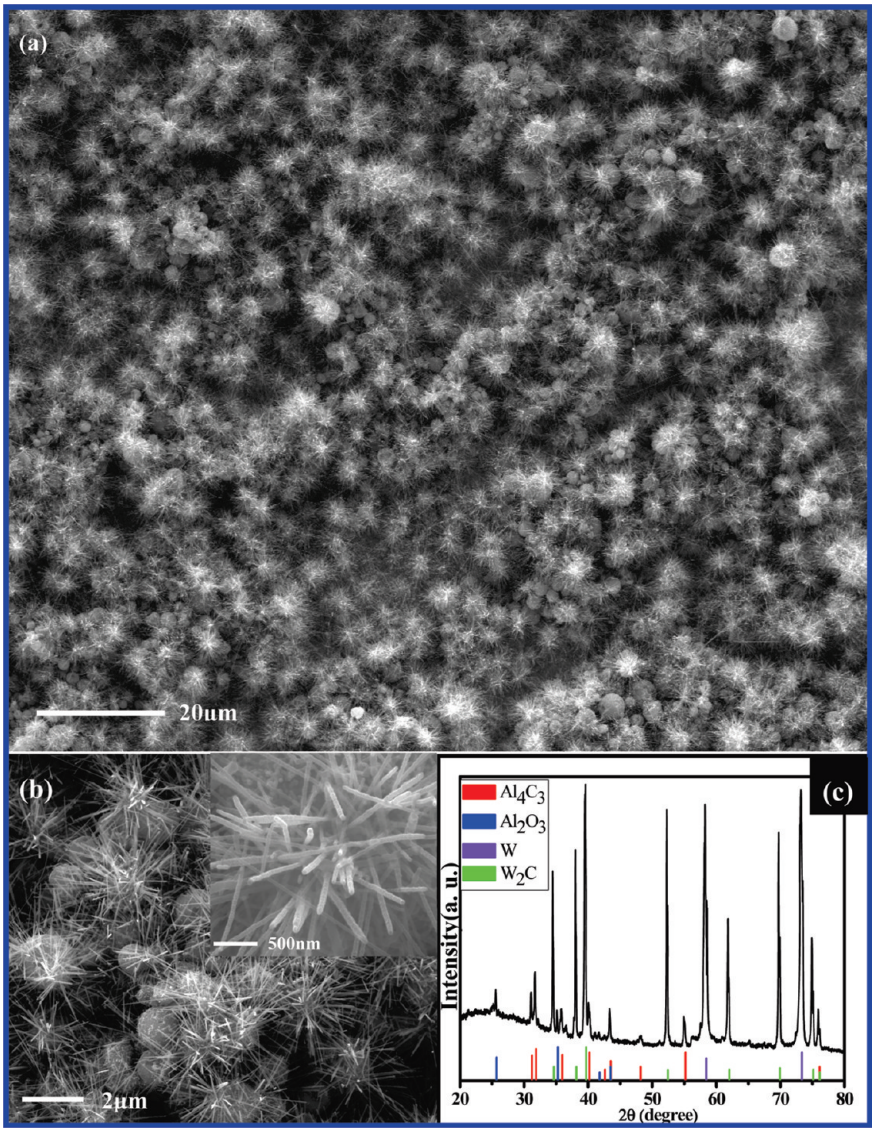


**Figure 2. Scanning electron microscopy (SEM) and X-ray diffraction (XRD) analysis of the sample. (a) Typical electron micrograph of $Al_4C_3$ microball-nanowire structure. (b) High-magnification SEM image of this novel microball-nanowire morphology. Inset showing a group of quasi-oriented nanowires grown on a single ball. (c) XRD pattern of the as-prepared sample. The colorful lines at the bottom correspond to the standard XRD pattern of *R*-$Al_4C_3$ (JCPDS No. 35-0799), $Al_2O_3$ (JCPDS No. 46-1212), W (JCPDS No. 04-0806), and $W_2C$ (JCPDS No. 35-0776).**

fluctuation of Al and O elemental content with the light and dark regions alteration, while the C signal nearly is uniform across the nanowire. Figure 4c and d show the line scan spectrum of a nanowire cross the radial dark gray and light domains, respectively. One can see that Al has a low and high intensity in the dark gray and light areas, respectively. The O and C elements have an obvious high content at the shell and core part, respectively. Based on the above analysis, we can see that the bright domain is significantly Al and C rich, suggesting it might be aluminum carbide, and the dark gray area is C rich, indicating it might be carbon in simple substance. As is seen, oxygen has a minimum around the central position, illustrating that the oxygen might be mainly incorporated into Al and form the alumina shell. It is well-known that the line scan EDX of the O and especially the C has detector-limited sensitivity, so elemental maps were acquired for a single nanowire, as shown in Figure 5.

Figure 5a is a typical STEM image of nanowires which displays similar contrast alteration morphology mentioned above and Figure 5b−d are elemental mapping images corresponding to Al, O, and C, respectively. From Figure 5b, one can see that Al signal is quasi-periodic across the whole nanowire. Figure 5c indicates that O elemental distribution is mainly concentrated in the shell part of the nanowire and D reveals that C element spread all over the nanowire. According to the above evidence, it is rational to speculate that the nanowire superstructures sheathed with a thin layer of alumina are composed of carbon and aluminum carbide.

Further structural characterization using TEM and selected area diffraction (SAD) is depicted in Figure 6. In detail, one can see that the dark and bright areas are single-crystalline structures and amorphous forms, respectively, which are shown in parts b, d, and e of Figure 6. According to the EDS mapping information (Figure 5) and SAD pattern (Figure 6c) of marked area in Figure 6b, it could be concluded that crystal $Al_4C_3$ and amorphous carbon make up of the superstructure nanowires. Electron diffraction reveals the growth direction of the crystal $Al_4C_3$ is along (0003), which has a *d*-spacing of 0.83 nm (Figure 6c). In addition, it is commonly discovered that the quasi-periodic nanowire superstructures are capped with $Al_4C_3$ nanolayers on the end (Figure 5a), which means that the $Al_4C_3$ cap would play an important role on electronic field emission. To obtain more detailed information of the novel structures, $Al_2O_3$ nanoshell is analyzed using HRTEM and EDS, as shown in Figure 7. Marked area in the HRTEM image exhibits trenchant lattice stripe phase which indicates the interplanar spacing of 0.45 nm based on Fourier transformation (inset of Figure 7b). EDS on area marked by circle in Figure 7b exhibits that only Al and O elements were detected. According to above analysis, we could conclude that crystal $Al_2O_3$ shell wraps the nanowires. The wrapping shell of crystal $Al_2O_3$ can significantly stop $Al_4C_3$ lattice from hydrolyzing, which do good to improve the stability of the sample.

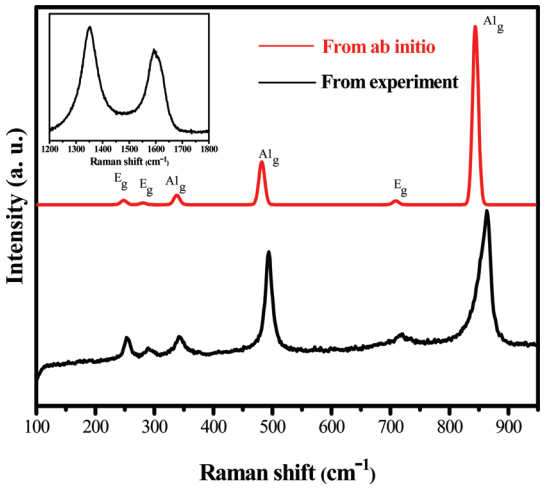


**Figure 3. Raman investigation with methods of *ab initio* and experimental measurement. Red line illustrates the result from theoretical calculation and black line is the practical testing spectra of the as-grown sample. Two curves have a good coincidence. Inset shows the D and G peaks for carbon signal from practical measurement.**

It is confirmed by Figure 8 that composition of the microballs is $Al_4C_3$. Typical low-magnification TEM images are shown in part (a) of Figure 8. Figure 8a shows that a microball combining with nanowires exhibits spiny ball morphology, which is consistent with the initial structure shown in SEM images of Figure 2. Compared to Figure 2, there are relative lacking nanowires on a microball, and this might be

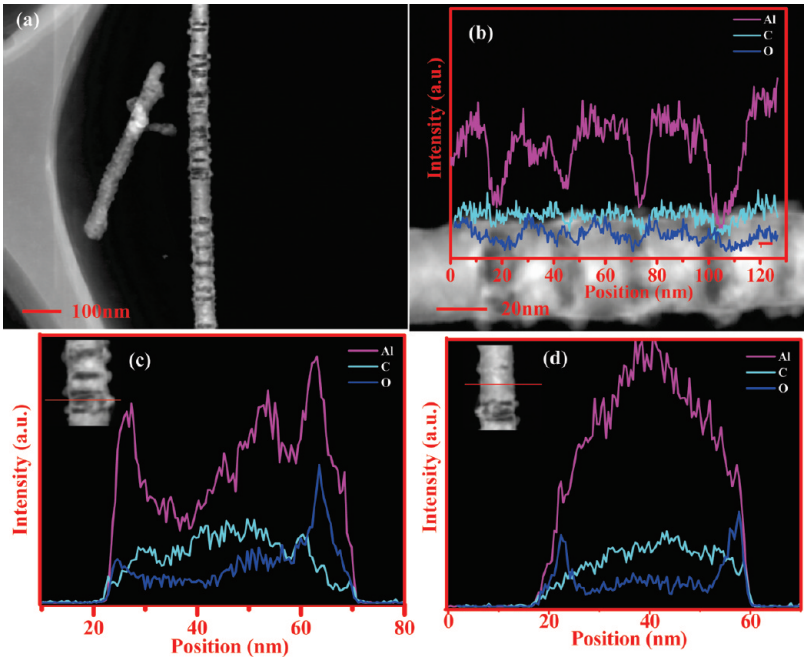


**Figure 4. Elemental analysis on an $Al_4C_3$ nanowire. (a) STEM image of a single nanowire used to analyze the elemental distribution. (b) ED line scanning spectroscopy of a length of crystal $Al_4C_3$-amorphous carbon alternatively stacked nanowire. Al and O elements exhibit an obvious periodic fluctuation. Amorphous area owns a low intensity of the Al and O elements, whereas C has a relatively constant intensity. (c) ED line scanning spectroscopy about the segment of amorphous carbon highlighted as a red line in the inset. Al and O exhibit a high content on the fringe and C owns a high intensity on the middle part. (d) Image showing the ED line scanning spectroscopy about the crystal $Al_4C_3$ section. Curves of Al and O elements obviously have peaks at the outskirt of the nanowire corresponding to the existence of $Al_2O_3$.**

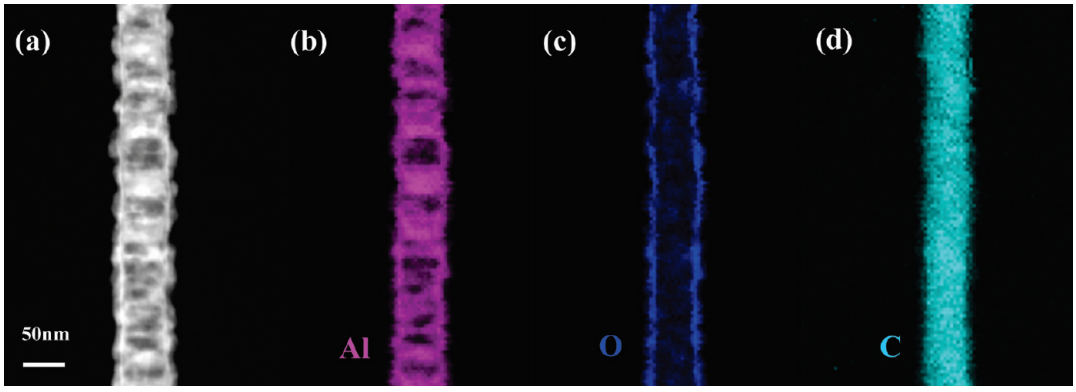


**Figure 5. (a) Typical STEM image of a single $Al_4C_3$ nanowire, which reveals a quasi-periodic alteration of image contrast in the lengthwise direction. (b−d) EDS elemental mapping images for the nanowire. Colored areas from B to D indicate Al element, O element, and C element enriched areas of the nanowire, respectively. Area with bright intensity represents a higher elemental concentration than an area with dark intensity.**

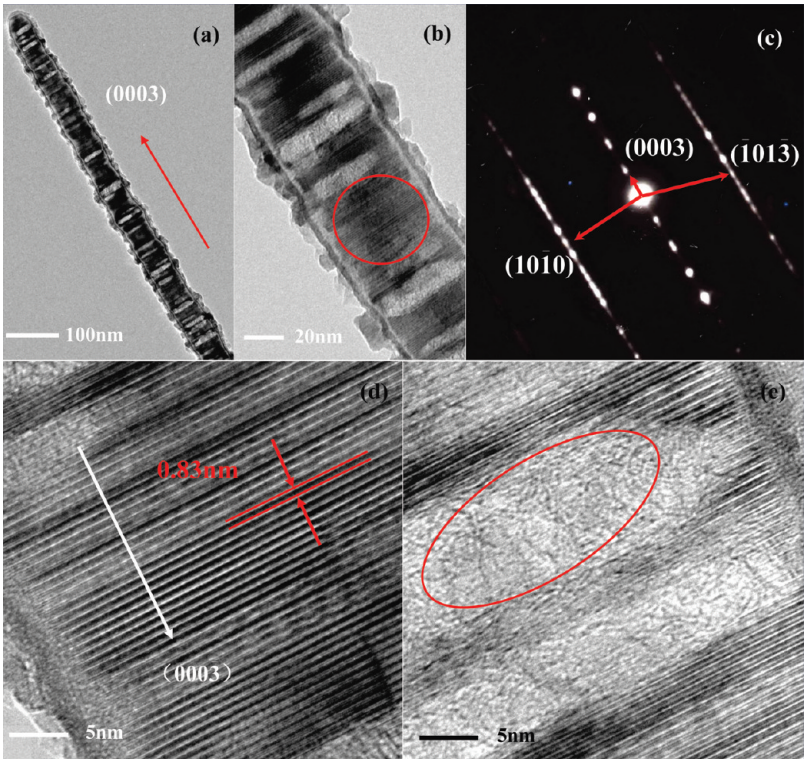


**Figure 6. Structure characterization of $Al_4C_3$ nanowires. (a, b) TEM images of a same nanowire in different magnification, which shows a lattice-amorphous alteration structures. (c) SAED (selected area electron diffraction) pattern from the marked area in (b). (d) High-resolution TEM (HRTEM) image of lattice segment of the nanowire, indicating a C-axial growth direction of $Al_4C_3$. (e) HRTEM image of the amorphous section.**

because most of nanowires have been broken down during the TEM sample preparation. Figure 8b and c show the SAD pattern and high-resolution TEM image, respectively. The SAD pattern is from the marked area in Figure 8a, which is mainly composed of two sets of fundamental patterns distinguished by solid and dotted red lines, indicating the twin-crystal structure. It implies that the microball has a polycrstal structure which composed of relatively large crystal grains. One set of the SAD patterns can be readily indexed as shown, exhibiting the hexagonal $Al_4C_3$ structure. Moreover, other discrete diffraction spots might result from the Al cluster inlaying randomly in the ball. Similar to $Al_4C_3$ nanowires, the HRTEM of the $Al_4C_3$ microball indicates the (0003) base plane. Figure 8d exhibits the line scan spectrum of the ball across a whole diameter, in which we can see the O element keeps a constant intensity, illustrating that the oxygen might be mainly incorporated into Al and form the $Al_2O_3$ shell, and the Al elemental content depends on the vertical thickness of the ball. However, the C element appears as a nonuniform content shown in the image, which can be attributed to the excessive carbon on the ball surface that might be the upper surface (exposure to

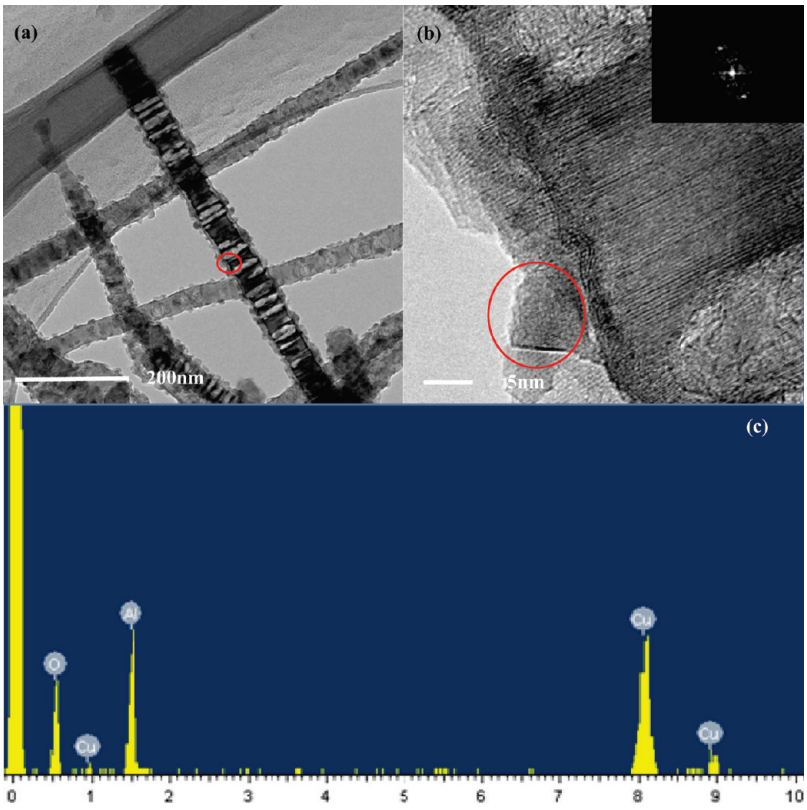


Figure 7. TEM analysis for the shell of nanowires. (a) A typical TEM image for a highlight nanowire. (b) HRTEM image for the marked area in A, in which shell lattice and $Al_4C_3$ lattice can be distinguished clearly. The inset is the Fourier Transform pattern for part of the shell. (c) EDS analysis for shell segment, in which only Al, O, and C elements are included and the O element exhibits a high intensity.

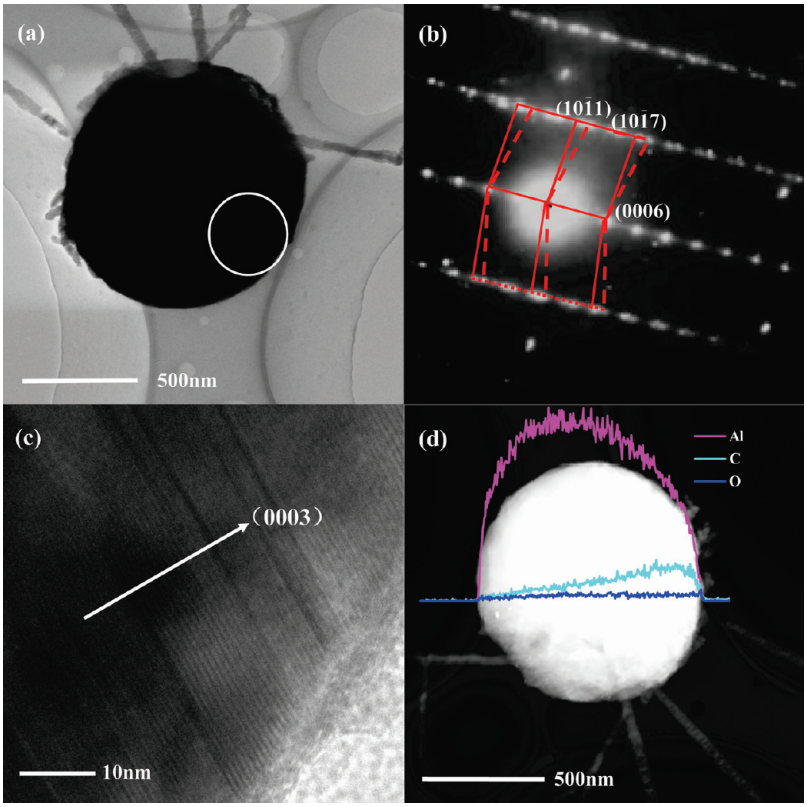


Figure 8. TEM characterization of $Al_4C_3$ microballs. (a) TEM image of a typical $Al_4C_3$ microball with a diameter of about 1 $\mu$m. (b) Selected area electron diffraction pattern shows a set of single-crystal diffraction points. (c) HRTEM image of the fringe section of the ball that shows the (0003) base plane reveals an $Al_2O_3$ surface layer several nanometers thick. (d) ED line scanning spectrum through a whole diameter of the ball. Al exhibits a highest intensity at the center and O keeps the same level.

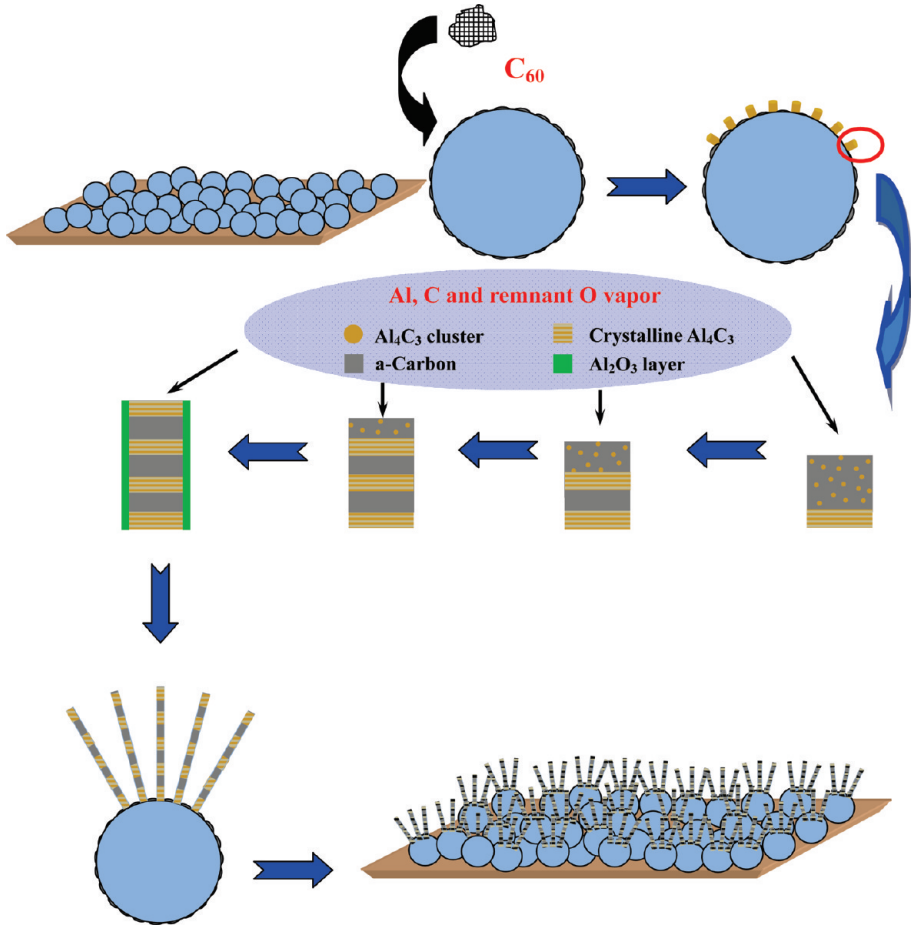


**Figure 9. Growth process proposed for the formation of carbon-in-$Al_4C_3$ nanowire superstructures (see main text for details).**

the growth atmosphere) of the microball, because more carbon would deposit on this surface part of the ball during the growth process. Based on the above analysis, one can conclude that the nanowire superstructure grown on the $Al_4C_3$ microball is composed of amorphous carbon quasi-periodic embedding in a single crystalline $Al_4C_3$ nanowire sheathed with a thin $Al_2O_3$ shell.

Based on these results, we suggest that the carbon-in-$Al_4C_3$ growth possibly follows a self-assembly mechanism as illustrated schematically in Figure 9. As mentioned in the Methods, we used $C_{60}$ as a solid carbon source. Compared with other carbon materials, $C_{60}$ possesses higher activity and lower sublimation temperature.[14] When the system is heated up to 350 °C, plenty of $C_{60}$ molecules will sublimate and deposit onto the Al microballs covered on W foil to form a high quality textured $C_{60}$ thin film, accompanying with the emergence of many nanoholes.[15] With the temperature increasing, the textured $C_{60}$ thin film will be prone to amorphization due to the existence of residual oxygen in the systems and subsequently react with Al to produce $Al_4C_3$ textured thin film, which covers the surface of the Al microball. After the temperature increases to above the melting point of Al, molten Al will be extruded quasi-ordered arrays *via* the nanoholes, which rapidly react with carbon vapor and form $Al_4C_3$ nanocylinders. As the temperature increase further, the gaseous carbon and gaseous Al are produced by the decomposition of $C_{60}$ and vaporizing of Al sheets, respectively. At high temperatures, the gaseous C and Al are transported to the $Al_4C_3$ nanocylinders mentioned above and form the hybrid of $Al_4C_3$(s) and amorphous carbon clusters due to the excess gaseous carbon. According to the classical theory of nucleation, the $Al_4C_3$ clusters are more inclined to nucleate at the boundaries of the nanocylinders and then grow up along them *via* Ostwald ripening to form carbon-in-$Al_4C_3$ nanowire superstructures. In the meantime, the gaseous carbon diffuses through the $Al_4C_3$ films already grown on Al microball substrates and reacts with molten Al and then forms $Al_4C_3$ microballs. During the nanostructures growth, when the carbon gets less and less, the C gaseous concentration will decrease to below the supersaturating in the substrate regions, which results in the nanowire superstructures stopping growth. On the other hand, in our experiment, a quantity of oxygen remains in the furnace due to the low vacuum condition. So, due to the relative low quantity of C atoms, the $O_2$ will have a chance to take part in the reaction with $Al_4C_3$ and yield the $Al_2O_3$ shell.

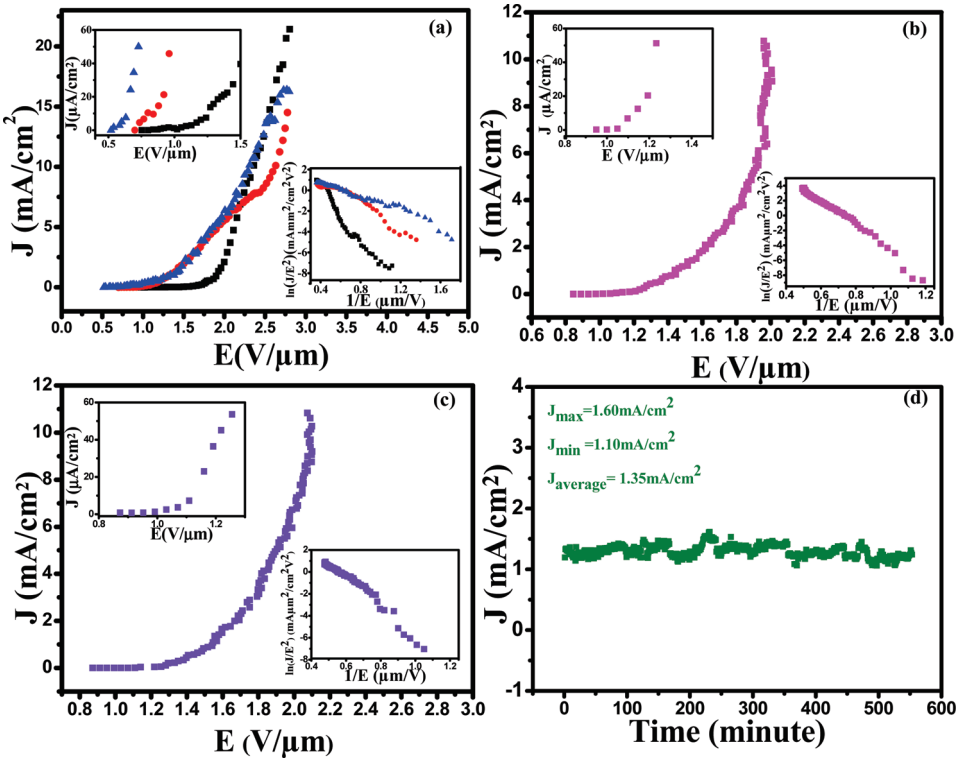


**Figure 10. Field emission characteristic of $Al_4C_3$ microball-nanowire emitter. (a) The dependence of field emission density *J vs* applied electric field strength *E* of the sample with a distance of 250 $\mu$m (emitting area 2.4 mm$^2$), in which the threshold fields are 2.29, 2.35, and 2.61 V/$\mu$m. Inset on upper left corner shows turn-on fields are 0.63, 0.82, and 1.25 V/$\mu$m. Inset on right bottom exhibits Fowler-Nordheim plots. (b, c) *J*−*E* curves from the sample with an emitting area of 0.1256 mm$^2$ on the other two emitting areas (with a distance of 225 and 250 $\mu$m, respectively). *F*−*N* plots and turn-on field are shown as corresponding insets. (d) Time dependence of emission current of the electron emitter at a central emission current density of about 1.3 mA/cm$^2$, and data are recorded once a minute.**

The field emission *I*−*V* characteristics of the as-synthesized sample was measured in a vacuum chamber at a pressure of $10^{-7}$ Torr at room temperature. Column-shaped stainless-steel probes with radii of 0.87 and 0.2 mm were used, respectively, as the anode. The fresh sample used as the cathode was stuck to a Cu plate by double-sided conductive carbon tape. In this condition, electrons can be transported to the $Al_4C_3$ structures through conductive W substrate and the carbon tape easily. In the measuring circuit, emission current was directly determined using Kethley 2400. The distance between the tip and the cathode was controlled by a digital micrometer controller and an optical microscope.

To investigate field emission uniformity, three separated regions of the same sample were tested using the anodes of different radii. For the first measuring point, three cyclic curves of emission current density *versus* electric field (*J*−*E*) for a typical carbon-in-$Al_4C_3$ structure are obtained using the anode with diameter of 1.74 mm, as shown in Figure 10a. The measured distance between anode and emitting surface was fixed at 250 $\mu$m. As expected from the $Al_4C_3$-based complex nanowires, excellent field emission properties have been observed in the three cycles, which exhibit very good repeatability. The electron emission turn-on field ($E_{to}$) and threshold field ($E_{thr}$), which are defined to be the macroscopic electric field required to generate a current density of 10 $\mu$A/cm$^2$ and 10 mA/cm$^2$, are at the range of 0.65−1.3 V/$\mu$m (top left corner of Figure 10a, inset) and 2.3−2.6 V/$\mu$m, respectively. The current density reaches as high as 20 mA/cm$^2$ at an electric field of 3.0 V/$\mu$m. The other two areas were tested using the anode with diameter of 0.4 mm. Parts (b) and (c) of Figure 10 show the current density as a function of the applied voltage for the second and third regions of the specimen, respectively. Figure 10b exhibits that the $E_{to}$ and $E_{thr}$ are 1.09 V/$\mu$m (see the top left corner of Figure 10b) and 2.2 V/$\mu$m under the distance of 225 $\mu$m. However, Figure 10c shows the *J*−*E* plot obtained from the third point with the distance of 250 $\mu$m, which indicates the $E_{to}$ and $E_{thr}$ are 1.1 V/$\mu$m (top left corner of Figure 10c) and 2.1 V/$\mu$m, respectively. All the areas show an excellent field emission property of this material. As far as we know, such low turn-on emission has not been reported before for emitters of any types (see Table 1). The very low electron emission fields for the sample imply that if it was used as the cathode in vacuum microelectrnic devices, high current density would be provided at a low voltage. Moreover, the wrapping shells of $Al_2O_3$ with several nanometers outside the nanowires can improve its stability toward

**TABLE 1. Comparison of Typical Fe between Carbon-in-$Al_4C_3$ Nanowire Superstructures and Others[a]**

| materials | turn-on field (V/$\mu$m) | threshold field (V/$\mu$m) |
|---|---|---|
| well-aligned carbon nanotubes[16] | 1.6 | 5 |
| diamond nanorods[17] | 1.3 | 2.9 |
| ZnS nanobelts[18] | 3.47 | >5.5 |
| B nanowires[19] | 5.1 | 11.5 |
| $TaSi_2$ nanowires[20] | 4−4.5 | 6.5 |
| $W_{18}O_{49}$ nanowires[21] | 2.6 ± 0.1 | 6.2 |
| oriented SiC nanowires[22] | 0.9 | 2.5−3.5 |
| Mo nanowires[23] | 2.2 | 6.24 |
| $MoO_2$ nanowires[23] | 2.4 | 5.6 |
| $MoO_3$ nanowires[23] | 3.5 | 7.65 |
| $Cu_2S$ nanowires[24] | 6.0 | ∼12 |
| tungsten whiskers[25] | 4.0 | |
| ZnO nanoneedles[26] | 2.5 | 4.0 |
| $Co_5Ge_7$ nanobelts and nanowires[27] | 1.6 | |
| AlN nanowires[28] | 6.0 | ∼9 |
| $Si_3N_4$ nanowires decorated with BN nanosheeets[29] | 4.2 | 4.4 |
| single-layer graphene films[30] | 2.3 | 5.2 |
| carbon-in-$Al_4C_3$ nanowire superstructures | 0.65−1.3 | 2.1−2.6 |

[a] Note: The turn-on field is defined as the electric field needed to obtain a current density of 10$\mu$A/cm$^2$, while threshold field is defined as the electric field needed to generate a current density of 10 mA/cm$^2$.

hydrolysis enormously. Therefore, it may be great used in flat panel display applications.

So, attracted field emission behavior can be attributed to the fantastic electron property of $Al_4C_3$ and the novel superstructure, as characterized above. As mentioned, similar to the alkali metals, $Al_4C_3$ is easy to give out electrons as the discrete $C^{4-}$. Furthermore, the alternative distribution of the crystal $Al_4C_3$ layer and amorphous carbon layer supply a fluent transport for electrons. In detail, first, as shown in TEM analysis, the c-axial distance of two adjacent carbon layers ranges from several nanometers to tens of nanometers, which is comparable to and even smaller than the mean free path of an electron in semiconductor, that is to say, free electrons can easily move in $Al_4C_3$ layer under high electronic field. Second, due to its alkali metals-like property, the $Al_4C_3$ layer is convenient to supply tunneling electrons through heterogeneous interface for the carbon layer which is electron lacking part. Additionally, conductive carbon layer can transfer electrons almost without resistance between $Al_4C_3$ layers. That is to say, the intervals of $Al_4C_3$ layers filled with amorphous carbon quasi-periodically form an excellent electron transport path which overcomes the disadvantages of $Al_4C_3$ as a nonconductive material at room temperature. After electrons emitted from the top of a nanowire, other electron can be supplied bottom up through the carbon-in-$Al_4C_3$ nanowire superstructures.

The field-emission data was analyzed using the Fowler-Nordheim (FN) model.[31] According to typical FN theory, the field emission current $J$ can be expressed in the following form:

$$J = A(\beta^2 E^2/\Phi)\exp(-B\Phi^{3/2}/\beta E)$$

where $A = 1.54 \times 10^{-10}$ in units of A (eV) V$^{-2}$, $B = 6.83 \times 10^7$ in units of (eV)$^{-3/2}$ V cm$^{-1}$, $\beta$ is the field enhancement factor, $E$ is the applied field ($E = V/d$), and $\Phi$ is the effect work function of the emission tip. By plotting $\ln(J/E^2)$ *versus* $1/E$, traditional FN plots can be obtained. Insets in the lower right corner of Figure 10a−c display FN plots of the corresponding $J$−$E$ curve. The linearity of FN curves implies that the field emission from the sample follows FN theory well.

Finally, we have measured the emission stability of the sample, which is critical for a cold-cathode material. Figure 10d is the emission current density *vs* time at constant applied field of 1.8 V/$\mu$m (the applied voltage was 450 V and the cathode−anode distance was 250 $\mu$m) for the carbon-in-$Al_4C_3$ nanowire superstructures on W foil. It is evident that the sample exhibits good emission current stability with a fluctuation less than 15% during a 9 h emission.

## CONCLUSIONS

In summary, we demonstrate that the strategy illustrated here provides a route to prepare $Al_4C_3$-based nanowire superstructures with excellent FE performance that are composed of $Al_4C_3$ nanowires embedding discrete a-C nanolayers with a thin shell layer of $Al_2O_3$. The carbon nanolayers, which act as an electronic conduction channel to the end of the nanowires that favor emission *via* electron tunneling from $Al_4C_3$ nanolayers, are vital to displaying the FE characteristic features of insulating $Al_4C_3$ for not providing enough electrons. The shell of crystal $Al_2O_3$ can significantly prevent $Al_4C_3$ lattice from hydrolyzing, which do good to improve the stability of the sample. In the technological field, finding such a composite material may open the way to new applications of $Al_4C_3$ ceramic in FE displays and vacuum microelectronic devices. Future work might focus on the patterned growth of carbon-in-$Al_4C_3$ nanowire arrays to further improve their field-emission performance.

## METHODS

The $Al_4C_3$ nanowire superstructures were synthesized in a conventional horizontal tube furnace, which is similar to that formerly used for synthesizing other 1D nanomaterials and nanostructures.[32−34] In detail, 12 mg commercially available $C_{60}$ powders (Peking University, China, 98%) and two Al sheets (10 × 10 × 1 mm$^3$, Shanghai Jingchui Reagent Co. China, 99.95%) were used as carbon and Al sources, respectively. A

tungsten (W) foil ($5 \times 5 \times 0.1$ mm$^3$, Alfa Aesar, 99.9%) covered with well-dispersed Al microballs (typical diameters of $1-2\ \mu$m) was used as substrate. The $C_{60}$ powders, Al sheets, and tungsten foil were loaded on an alumina slice with the uniform interval. The alumina slice was then positioned at the center of a half-sealed alumina tube. The whole assembly was finally pushed into a ceramic tube of a tube furnace pumped by a rotary pump, as shown in Figure 1b. Before the heating process, the whole system was purged by high-purity Ar (99.99%) three times, and then the system was heated to 1310 °C at the rate of 5 °C per minute and held for an hour. When heated to 350 °C, high-purity Ar with a constant flow of 50 sccm (standard cubic centimeters per minute) and a pressure of 50 KPa was introduced into the system. The temperature where the nanostructures were grown was controlled to be about 1290−1310 °C due to the temperature gradient in the ceramic tube.

Detailed morphological and structural characterizations were carried out by field emission scanning electron microscopy (FESEM), X-ray diffraction (XRD), high-resolution transmission electron microscopy (HR-TEM, JEOL2010, operated at 200 kV accelerating voltage at room temperature), scanning TEM (STEM), and STEM X-ray energy dispersive spectroscopy (EDS).

*Acknowledgment.* The National Nature Science Foundation of China (50772135, U0734004) and Nature Science Foundation of Gangdong province (8251027501000014) and Doctoral Foundation (200805580018) supported this work.

## REFERENCES AND NOTES


1. Xu, N. S.; Huq, S. E. Novel Cold Cathode Materials and Applications. *Mater. Sci. Eng., R* **2005,** *48*, 47–189.
2. Zhirnov, V. V.; Wojak, G. J.; Choi, W. B.; Cuomo, J. J.; Hren, J. J. Electronic Structure and Electron Emission of Lithium-Containing Amorphous Hydrogenated Carbon Films. *J. Vac. Sci. Technol., A* **1997,** *15*, 1733–1738.
3. Qiu, C.; Metselaar, R. Solubility of Carbon in Liquid Al and Stability of $Al_4C_3$. *J. Alloys Compd.* **1994,** *216*, 55–60.
4. Arik, H. Production and Characterization of In Situ $Al_4C_3$ Reinforced Aluminumbased Composite Produced by Mechanical Alloying Technique. *Mater. Des.* **2004,** *25*, 31–40.
5. Liu, Y. H.; Liu, X. F.; Bian, X. F. Grain Refinement of Mg−Al Alloys with $Al_4C_3$−SiC/Al Master Alloy. *Mater. Lett.* **2004,** *58*, 1282–1287.
6. Besterci, M.; Ivan, J.; Pesek, L.; Velgosová, O.; Hvizdos, P. Damage Mechanism of Al−12$Al_4C_3$. *Mater. Lett.* **2004,** *58*, 867–870.
7. Park, J. K.; Lukas, J. P. Moisture Effect on $SiC_p$/6061 Al MMC: Discussion of Interfacial $Al_4C_3$. *Scr. Mater.* **1997,** *37*, 511–516.
8. Greenwood, N. N.; Earnshaw, A. *Chemistry of the Elements*; Pergamon: Oxford, 1984; pp 318−322.
9. Solozhenko, V. L.; Kurakevych, O. O. Equation of State of Aluminum Carbide $Al_4C_3$. *Solid State Commun.* **2005,** *133*, 385–388.
10. Kawazoe, H.; Yasukawa, M.; Hyodo, H.; Kurita, M.; Yanagi, H.; Hosono, H. H. P-type Electrical Conduction in Transparent Thin Films of $CuAlO_2$. *Nature* **1997,** *389*, 939–942.
11. Noh, M.; Kwon, Y.; Lee, H.; Cho, J.; Kim, Y.; Kim, M. G. Amorphous Carbon-Coated Tin Anode Material for Lithium Secondary Battery. *Chem. Mater.* **2005,** *17*, 1926–1929.
12. Giannozzi, P.; Baroni, S.; Bonini, N.; Calandra, M.; Car, R.; Cavazzoni, C.; Ceresoli, D.; Chiarotti, G. L.; Cococcioni, M.; Dabo, I.; *et al.* QUANTUM ESPRESSO: A Modular and Open-Source Software Project for Quantum Simulations of Materials. *J. Phys.: Condens. Matter.* **2009,** *21*, 1–19.
13. Zhu, Y.; Matsumoto, A.; Senkowicz, B. J.; Kumakura, H.; Kitaguchi, H.; Jewell, M. C.; Hellstrom, E. E.; Larbalestier, D. C.; Voyles, P. M. Microstructures of SiC Nanoparticle-Doped $MgB_2$ /Fe Tapes. *J. Appl. Phys.* **2007,** *102*, 013913.
14. Dresselhaus, M. S.; Dresselhaus, G.; Eklund, P. C. *Science of Fullerenes and Carbon Nanotubes*; Academic: San Diego, 1996; Chap 5, and references therein .
15. Katz, E. A.; Faiman, D.; Shtutina, S.; Isakina, A. Deposition and Structural Characterization of High Quality Textured $C_{60}$ Thin Films. *Thin Solid Film* **2000,** *368*, 49–54.
16. Murakami, H.; Hirakawa, M.; Tanaka, C.; Yamakawa, H. Field Emission from Well-Aligned, Patterned, Carbon Nanotube Emitters. *Appl. Phys. Lett.* **2000,** *76*, 1776–1778.
17. Shang, N. G.; Papakonstantinou, P.; Wang, P.; Zakharov, A.; Palnitkar, U.; Lin, I. N.; Chu, M.; Stamboulis, A. Self-Assembled Growth, Microstructure, and Field-Emission High-Performance of Ultrathin Diamond Nanorods. *ACS Nano* **2009,** *3*, 1032–1038.
18. Fang, X. S.; Bando, Y.; Shen, G. Z.; Ye, C. H.; Gautam, U. K.; Costa, P. M. F. J.; Zhi, C. Y.; Tang, C. C.; Golberg, D. Ultrafine ZnS Nanobelts as Field Emitters. *Adv. Mater.* **2007,** *19*, 2593.
19. Liu, F.; Tian, J. F.; Bao, L. H.; Yang, T. Z.; Shen, C. M.; Lai, X. Y.; Xiao, Z. M.; Xie, W. G.; Deng, S. Z.; Chen, J.; *et al.* Fabrication of Vertically Aligned Single-Crystalline Boron Nanowire Arrays and Investigation of Their Field-Emission Behavior. *Adv. Mater.* **2008,** *20*, 2609–2615.
20. Chueh, Y. L.; Ko, M. T.; Chou, L. J.; Chen, L. J.; Wu, C. S.; Chen, C. D. $TaSi_2$ Nanowires: A Potential Field Emitter and Interconnect. *Nano Lett.* **2006,** *6*, 1637–1644.
21. Li, Y. B.; Bando, Y.; Globerg, D. Quasi-Aligned Single-Crystalline $W_{18}O_{49}$ Nanotubes and Nanowires. *Adv. Mater.* **2003,** *15*, 1294–1296.
22. Pan, Z. W.; Lai, H. L.; Au, F. C. K.; Duan, X. F.; Zhou, W. Y.; Shi, W. S.; Wang, N.; Lee, C. S.; Wong, N. B.; Lee, S. T.; *et al.* Oriented Silicon Carbide Nanowires: Synthesis and Field Emission Properties. *Adv. Mater.* **2000,** *12*, 1186–1190.
23. Zhou, J.; Xu, N. S.; Deng, S. Z.; Chen, J.; She, J. C.; Wang, Z. L. Large-Area Nanowires Arrays of Molybdenum and Molybdenum Oxide: Synthesis and Field Emission Properties. *Adv. Mater.* **2003,** *15*, 1835–1840.
24. Chen, J.; Deng, S. Z.; Xu, N. S.; Wang, S. H.; Wen, X. G.; Yang, S. H.; Yang, C. L.; Wang, J. N.; Ge, W. K. Field Emission from Crystalline Copper Sulphide Nanowire Arrays. *Appl. Phys. Lett.* **2002,** *80*, 3620–3622.
25. Wang, S. L.; He, Y. H.; Fang, X. S.; Zou, J.; Wang, Y.; Huang, H.; Costa, P. M. F. J.; Song, M.; Huang, B. Y.; Liu, C. T.; *et al.* Structure and Field-Emission Properties of Sub-Micrometer-Sized Tungsten-Whisker Arrays Fabricated by Vapor Deposition. *Adv. Mater.* **2009,** *21*, 2387.
26. Li, Y. B.; Bando, Y.; Golberg, D. ZnO Nanoneedles with Tip Surface Perturbations: Excellent Field Emitters. *Appl. Phys. Lett.* **2004,** *84*, 3603–3605.
27. Yoon, H.; Seo, K.; Bagkar, N.; In, J.; Park, J.; Kim, J.; Kim, B. Vertical Epitaxial $Co_5Ge_7$ Nanowire and Nanobelt Arrays on a Thin Graphitic Layer for Flexible Field Emission Displays. *Adv. Mater.* **2009,** *21*, 4979–4982.
28. Shi, S. C.; Chen, C. F.; Chattopadhyay, S.; Chen, K. H.; Chen, L. C. Field Emission from Quasi-Aligned Aluminum Nitride Nanotips. *Appl. Phys. Lett.* **2007,** *87*, 073109–073111.
29. Zhu, Y. C.; Bando, Y.; Yin, L. W.; Golberg, D. Field Nanoemitters: Ultrathin BN Nanosheets Protruding from $Si_3N_4$ Nanowires. *Nano Lett.* **2006,** *6*, 2982–2986.
30. Wu, Z. S.; Pei, S. F.; Ren, W. C.; Tang, D. M.; Gao, L. B.; Liu, B. L.; Li, F.; Liu, C.; Cheng, H. M. Field Emission of Single-Layer Graphene Films Prepared by Electrophoretic Deposition. *Adv. Mater.* **2009,** *21*, 1756–1760.
31. Fowler, R. H.; Nordheim, L. W. Electron Emission in Intense Electric Fields. *Proc. R. Soc. A* **1928,** *119*, 173–181.
32. Cui, H.; Sun, Y.; Yang, G. Z.; Chen, J.; Jiang, D.; Wang, C. X. Template- and Catalyst-Free Synthesis, Growth Mechanism and Excellent Field Emission Properties of Large Scale Single-Crystalline Tubular $\beta$-SiC. *Chem. Commun.* **2009,** 6243–6245.
33. Yang, G. Z.; Cui, H.; Sun, Y.; Gong, L.; Chen, J.; Jiang, D.; Wang, C. X. Simple Catalyst-Free Method to the Synthesis of $\beta$-SiC Nanowires and Their Field Emission Properties. *J. Phys. Chem. C* **2009,** *113*, 15969–15973.
34. Sun, Y.; Cui, H.; Yang, G. Z.; Huang, H.; Jiang, D.; Wang, C. X. The Synthesis and Mechanism Investigations of Morphology Controllable 1-D SiC Nanostructures via a Novel Approach. *CrystEngComm* **2010,** *12*, 1134–1138.